ACS APPLIED MATERIALS & INTERFACES

Research Article

www.acsami.org

Enhanced Photovoltaic Performance of Semiconductor-Sensitized ZnO–CdS Coupled with Graphene Oxide as a Novel Photoactive Material

Dipankar Barpuzary and Mohammad Qureshi*

Materials Science Laboratory, Department of Chemistry, Indian Institute of Technology Guwahati, Assam-781039, India

Supporting Information

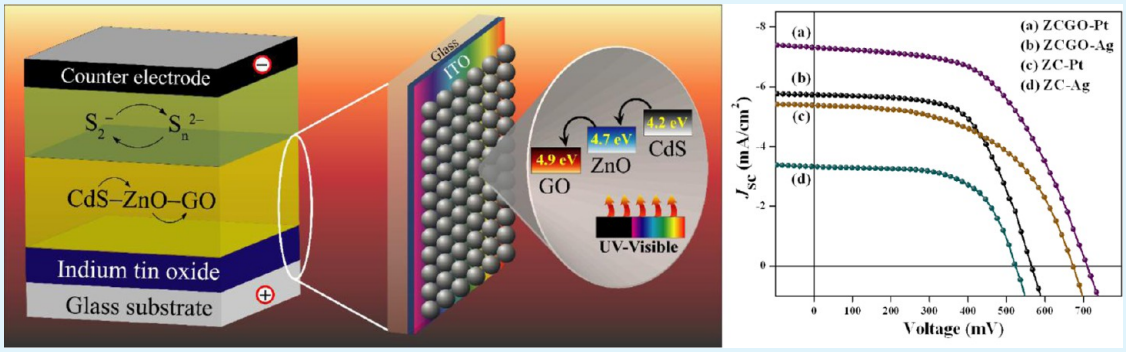

ABSTRACT: We report, for the first time, a ternary hybrid composite of ZnO, CdS, and graphene oxide (GO) as a one-coat paintable solution in performing the role of a photoanode for the semiconductor-sensitized solar cell, wherein hierarchical ZnO–CdS heteroarrays are embedded onto the GO sheets. The photoconversion properties of the hybrid ternary-system-based photoanodes are evaluated in the photovoltaic devices having Pt and Ag as the counter electrodes with sulfide/polysulfide redox couple as the electrolyte. Power conversion efficiency (PCE) of ~2.82% has been achieved with a short-circuit current density (J_{sc}) of ~7.3 mA/cm^2, a maximum open-circuit voltage (V_{oc}) of 703 mV, and a fill factor (FF) of 54% for the photovoltaic cell with Pt as a counter electrode. The identical hybrid photoanode against the Ag counter electrode resulted in the following values: PCE ≈ 1.96%, J_{sc} ≈ 5.7 mA/cm^2, V_{oc} ≈ 565 mV, and 63% FF. The band position proximity of CdS, ZnO, and GO in the proposed ternary system facilitates an efficient electronic interactions thereby promoting the electron transport within CdS–ZnO–GO. The hierarchically grown CdS nanorods over ZnO nanoparticle act as the sensitizer for ZnO, enhancing the visible light harvesting ability. The loading of 1.0 wt % of GO to ZnO–CdS results in enhanced separation of photogenerated electrons and holes within the photoactive layer, thereby improving the photovoltaic performance. The electronic interactions of GO to ZnO–CdS is evident from the drastic quenching of fluorescence, reduced exciton lifetime and Raman scattering measurements. In order to study the effect of GO in the photovoltaic performance, we have compared our result with the photoelectrical parameters of the devices fabricated using the binary ZnO–CdS composite as GO-free photoanodes.

KEYWORDS: *photovoltaics, semiconductor-sensitized solar cell, hybrid ZnO–CdS–GO photoanode, time-resolved photoluminescence, electronic interaction, 1-D nanostructures*

1. INTRODUCTION

Semiconductor-sensitized solar cell (SSSC) fabrication and production have successively gained the academic and technological prominence among the researchers for their progressive development of photovoltaic power generation utilizing solar energy. Inorganic semiconductor nanomaterials with their favorable band-gap alignment, tunable size- and shape-dependent absorption properties, and the capability for efficient charge transfer in their composites invoke them as the emerging candidates to generate photovoltaic assemblies.[1,2] Enormous efforts and techniques have been devoted to develop promising energy-conversion-efficient solar cells based on either dye- or semiconductor-sensitized concepts.[3−9] Although very high, the efficiency of conventional dye-sensitized solar cell decreases with time as the dye starts to degrade under full solar irradiation. The SSSC, where the use of semiconductors give more stable configuration with respect to dye degradation, can be utilized to attain high visible light harvesting capability, high electron mobility of semiconductor (ZnO, TiO_2), and faster charge transport.[10−14] The coupling of nanostructured semiconductors, depending on the band edge alignments, is one of the practical solutions to achieve better device performance due to facile electron transport, enhanced surface area for optical absorption, and reduced optical reflection, compared to the

Received: August 7, 2013
Accepted: October 23, 2013
Published: October 23, 2013

Scheme 1. Schematic of the Solar Cell ITO/ZnO−CdS−GO (∼12 μm)/Pt; Magnified View Shows the Electron Transfer Pathway within the Ternary ZnO−CdS−GO Photoactive Layer

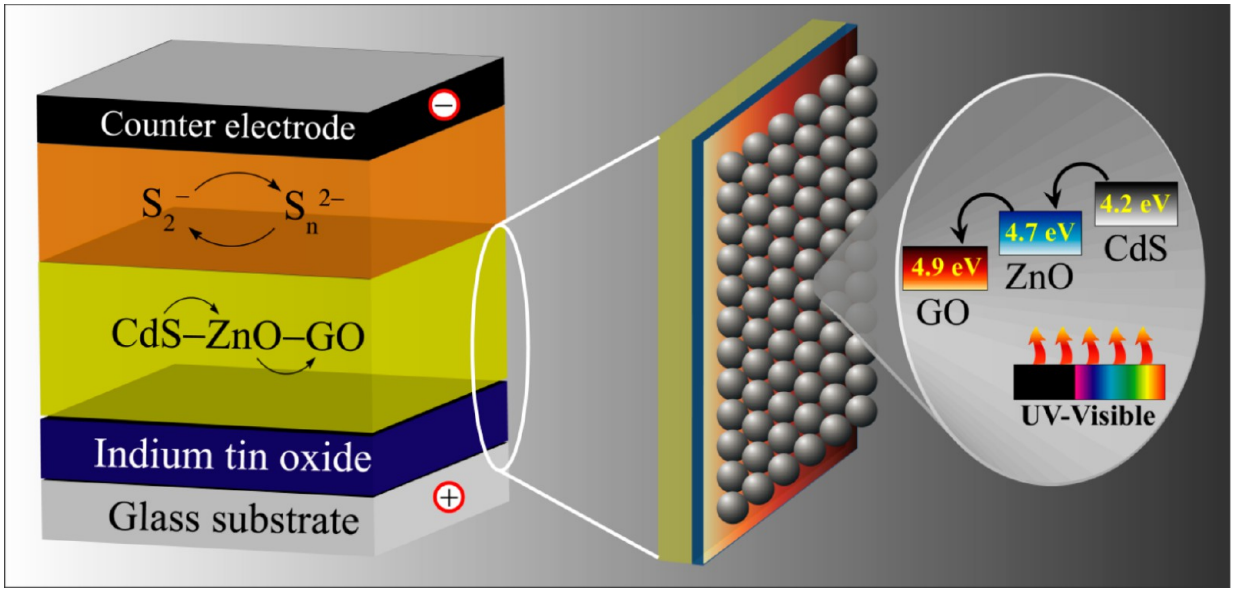

planar structures.[15−17] A rich variety of metal oxide nanostructures based on the wide range of synthetic routes can lead to generate the combination of wide- and narrow-band gap semiconductor heteroarrays. Designing hierarchical one-dimensional (1D) core−shell hetero assembly is one such critical approach. The major challenge to improve the semiconductor coupled-device performance is confined on the efficient physical separation and migration of the photogenerated electrons and holes under photoexcitation. Moreover, the introduction of graphene oxide (GO) to the system is a prominent technique to facilitate the charge separation and transfer processes.[18,19] In essence, the superior electronic interacting ability of GO with semiconductors is presently an issue of significant importance to explore and generate composite systems for photovoltaics.[20,21] Although the structural and chemical inhomogeneity of GO makes it complicated to define the electronic band gap,[22] theoretical and experimental evidence suggest the presence of a band gap defined by the sp^2/sp^3 domains.[23] Inorganic semiconductors coupled with graphene/GO have shown vast potential applications to attain efficient solar energy conversion, photocurrent generation, catalysis, and fuel cells.[24,25] The electronic interaction of the semiconductor or metal particles to graphene has been utilized to act their composites as energy storage materials (Li-ion battery anodes and capacitors) as well as for photocatalytic hydrogen generation.[26] Moreover, ternary inorganic−organic−GO hybrids have been used to achieve high-performance photovoltaic devices, because of higher photon-to-current conversion efficiency (∼70%).[27]

Herein, we introduce the idea to generate enhanced photocurrent by designing a new hierarchical ZnO−CdS−GO composite as the photoanode. Essentially, the faster electron transport capability of ZnO is responsible for its extensive application in photovoltaics.[28−30] However, the serious limitation of ZnO for solar cell application is due to its poor absorptivity in the visible region. Surface modification of ZnO via coupling with a narrow-band gap inorganic semiconductor (CdS, CdSe) is a recognized technique for better light absorption and, hence, the device performance.[31−35] ZnO electrodes can be sensitized with CdS or CdSe quantum dot (QD) to enhance light harvesting capacity by chemical bath deposition and successive ion layer adsorption and reaction (SILAR) methods, where the sensitizers are directly grown onto ZnO surface.[36,37] However, the thicker QD layer limits the electron transport in the devices bceause of charge hopping, which could be overcome by loading GO or reduced-GO (RGO) to the semiconductor. Present work manifests the synthesis[38] of hierarchical core−shell heterosystem consisting of ZnO−CdS with 1.0 wt % GO loading for improved photovoltaic performance of hybrid ZnO−CdS−GO over ZnO−CdS photoanode, wherein CdS is impregnated directly onto the ZnO for the desired light sensitization in the heteroarrays. Previous work in our laboratory has shown the mechanistic influence of effective charge transfer and enhanced light absorption in the synthesized ZnO−CdS heterosystem, because of the impregnated growth of CdS over ZnO.[39] This approach offers a direct, fast, controllable, and efficient charge transport/separation through the radial versus axial direction, because of the one-dimensional (1D) morphology of the components.[40] In another report, we have shown the unique feature of GO as an excellent electron collector, as well as transport material for efficient separation of the photogenerated electron−hole pairs in its composite with ZnO−CdS.[19] It should be noted that both GO and RGO can be implied as an excellent electron acceptor material to couple with the semiconductors. However, Lightcap and Kamat have reported better electron-consuming capacity of GO over RGO, depending on the oxidation state and higher photoluminenscence (PL) quenching efficiency of GO than RGO.[37] The better quenching response of GO has also evidenced the higher interactive nature of GO, compared to RGO. The key advantage behind the introduction of ternary ZnO−CdS−GO in devices is to simultaneously achieve the enhanced photosensitization of wide-band-gap ZnO (∼3.7 eV) by CdS (∼2.5 eV) and the efficient electron transfer within the components, as shown in Scheme 1. The electronic interactions between GO and binary ZnO−CdS in the ternary hybrid ZnO−CdS−GO composites, synthesized by the hydrothermal treatment, is confirmed by

steady-state fluorescence, time-resolved photoluminescence (TRPL), exciton lifetime and Raman scattering studies, as discussed in the later stage.

The devices are fabricated by coating the ZnO−CdS−GO and ZnO−CdS paste onto the indium tin oxide (ITO)-coated glass substrates to act as the photoanodes, whereas Pt and Ag played the role of counter electrodes. Electrolyte function in the photovoltaic is initiated by introducing a sulfide/polysulfide (S_2^-/S_n^{2-}) redox couple, which is prepared by dissolving S (2M) and Na_2S (2M) in water. Scheme 1 shows a magnified view of ZnO−CdS−GO composite layer of the device.

2. EXPERIMENTAL SECTION

2.1. Materials Preparation. All the chemicals were purchased from Merck and used as received without further purification. Bare ZnO nanoparticles (NPs), CdS nanorods (NRs), and graphene oxide (GO), as well as ZnO−CdS and ZnO−CdS−GO composites, were synthesized following the protocol reported by our group.[18,38,39]

2.1.1. Synthesis of ZnO Nanoparticles. $ZnCl_2$ (5.5 g, 40 mmol) was dissolved in 200 mL of distilled water. An aqueous solution of 5 M NaOH (4 mL) was then added dropwise over a period of 15 min with gentle stirring at 90 °C. The heating and stirring were continued for another 60 min. The reaction mixture was cooled to room temperature, separated the ZnO NPs via the sedimentation method, and the supernatant dispersion was washed several times with water. The complete removal of NaCl was tested by $AgNO_3$ solution. The purified ZnO NPs were dispersed in isopropanol under ultrasonic treatment for a period of 10 min to resist agglomeration, collected by centrifugation, followed by calcination at 350 °C in a muffle furnace for 3 h. The ZnO NPs were synthesized with a practical yield of ∼52%.

2.1.2. Synthesis of CdS Nanorods. $Cd(CH_3COO)_2{\cdot}2H_2O$ (2.39 g, 9 mmol) and thioglycolic acid (1.0 mL, 9 mmol) were mixed in ethylenediamine (10 mL) and stirred for 30 min. The synthesis of CdS NRs was completed by applying the hydrothermal treatment for 7 h at 140 °C. The solid sample obtained was separated by centrifugation and washed three times with distilled water and ethanol each. Finally, the sample was dried at 60 °C for 2 h in an electronic oven. The obtained yield of CdS NRs was found to be ∼48%.

2.1.3. Synthesis of Graphene Oxide. Graphene oxide (GO) was synthesized from graphite, using a modified Hummer's method.[41] Typically, 187 mL of concentrated H_2SO_4 was added to a mixture of 2.5 g of graphite and 1.87 g of $NaNO_3$ under gentle stirring in an ice bath, followed by the addition of 11.25 g of $KMnO_4$ over 1 h. The mixture was continuously stirred for another 2 h in an ice bath. The reaction mixture was subjected to vigorous stirring at 35 °C for 7 days. Then, 350 mL of 5 wt % H_2SO_4 aqueous solution was added slowly under continuous stirring and the temperature was increased rapidly to 98 °C and stirred for 2 h. Again the temperature was reduced to 60 °C and 4.7 mL of H_2O_2 (48 wt % aqueous solution) was added to remove the unreacted $KMnO_4$. The reaction mixture was then allowed to cool to room temperature and stirred for 2 h. The undesired ions and other inorganic components in the solution were then purified by centrifugation. A 1000 mL aqueous solution of 3 wt % H_2SO_4/0.5 wt % H_2O_2 was added to the precipitate and sonicated for 1 h. The impurities were then removed by centrifugation at 10 000 rpm for 20 min. Again, the sonication and centrifugation was performed three times. The same procedure was then repeated using 1000 mL of a 3 wt % HCl aqueous solution. After removing the impurities, GO was extracted in distilled water by ultrasonic treatment. The GO aqueous solution was dried in a vacuum oven at 50 °C to obtain the GO sheets (1.7 g).

2.1.4. Synthesis of ZnO−CdS and ZnO−CdS−GO Composites. For the synthesis of ZnO−CdS, the growth of CdS NRs was performed on the ex-situ-generated ZnO by simple hydrothermal strategy. First, ZnO NPs (3 mmol) were dispersed in 10 mL of water under an ultrasonic bath for 30 min. Thioglycolic acid (1 mL, 9 mmol) was added and stirred for 30 min, so that the S^{2-} ions (Lewis base) preferably attach to the ZnO surface due to the Lewis acidity center on Zn. Further addition of an aqueous solution of $Cd(CH_3COO)_2{\cdot}2H_2O$ (2.39 g, 9 mmol) with 30 min of continuous stirring persuaded the formation of CdS colloidal particles over ZnO. These saturated CdS particles then acted as the seeds for crystal growth of CdS NRs over ZnO from the supersaturated vapors of Cd^{2+} and S^{2-} under hydrothermal treatment for 48 h at 140 °C. The as-synthesized ZnO−CdS composite was repeatedly washed with water and ethanol several times and then collected by centrifugation at 5000 rpm. The solid was then dried in a vacuum oven at 50 °C for 4 h.

For the synthesis of ZnO−CdS−GO, first, GO (1.0 wt %, with respect to ZnO−CdS to be synthesized) was dispersed in 10 mL of water under ultrasonic bath for 1 h at 70 W at room temperature. Then, ZnO NPs (3 mmol), $Cd(CH_3COO)_2{\cdot}2H_2O$ (2.39 g, 9 mmol), and thioglycolic acid (1 mL, 9 mmol) were added and the same exact procedure for ZnO−CdS was repeated. The as-synthesized ZnO−CdS−GO composite was then washed with water and ethanol several times and collected by centrifugation at 25 000 rpm. The solid was then dried in a vacuum oven at 50 °C for 4 h. The yields of ZnO−CdS and ZnO−CdS−GO are found to be ∼57% and ∼53%, respectively.

2.1.5. Material Characterization. Powder X-ray diffraction (XRD) measurements to analyze the XRD patterns were performed using Bruker D8 Avance X-ray diffractometer with Cu Kα (λ = 1.54 Å) at an operating voltage of 40 kV and an operating current of 40 kA. The scan rate was fixed at 0.1°/s to record the XRD patterns for the 2θ range of 5°−70°. The ultraviolet−visible light (UV-vis) diffuse-reflectance absorption (DRS) spectra were recorded in a JASCO Model V-650 spectrophotometer equipped with a 150-nm integrating sphere and $BaSO_4$ internal standard. The surface morphology of the samples was investigated using scanning electron microscopy (SEM) on a LEO Model 1430vp instrument operated at 10−15 kV. A cross-sectional image of the photoanode of the solar cell was studied by field-emission scanning electron microscopy (FESEM) using a Zeiss (Gemini) instrument operated at 5 kV. The transmission electron microscopy (TEM) measurements were performed on a JEOL JEM 2100 microscope operating at 200 kV. Photoluminescence (PL) studies were performed using Horiba−Jobin Yvon Fluoromax 4 spectrophotometer. The TRPL experiments to determine the exciton lifetimes were performed using a LifeSpec II Edinburgh instrument with a lamp frequency of 5 MHz. A neodymium-doped yttrium aluminum garnet (Nd:YAG) laser with an excitation wavelength of 405 nm was used to excite the samples at a temperature of 23 °C. The laser micro-Raman spectroscopic measurement was conducted in a Horiba LabRAM HR spectrometer equipped with a He−Ne laser that has an excitation wavelength of 514.5 nm. The sample preparation for the analysis was carried out by placing the solid powder between two glass slides and then pressure was applied. The thin films thus obtained were then analyzed within the scan range of 100−2000 cm^{-1}. The thickness measurements for all the pasted/deposited layers of the solar cells were conducted using a Veeco Model Dektak 150 surface profilometer. The current density−voltage (J−V) measurements for the device were recorded using a Keithley Sourcemeter series 2420 in darkness and with 100 mW/cm^2 AM 1.5G of solar spectrum illumination. The intensity of the 450 W arc lamp fitted with Newport ORIEL Sol3A solar simulator was calibrated by a standard Si photovoltaic cell. Incident photon-to-current conversion efficiency (IPCE) measurement was performed by standard silicon and germanium diode calibrated Newport ORIEL IQE-200 fitted with 250 W quartz tungsten halogen lamp. The monochromatic light was illuminated through a Cornerstone monochromator and then allowed to pass through a chopper and the signal was finally amplified by a Merlin lock-in amplifier unit.

2.1.6. Device Fabrication and Characterization. For the device fabrication, ITO substrates having a sheet resistance of 8−10 Ω/cm^2 (Delta Technologies, Ltd., USA) were cleaned by soap solution and distilled water, followed by ultrasonic treatment for 15 min in isopropanol and acetone. The substrates were taken out from the solvent, dried by blowing argon gas, and then subjected to ozone treatment for 30 min at 60 °C in a Novascan UV/Ozone Probe chamber prior to use. Scotch tape was fixed to the edges of the ITO substrate to get an active area of ∼1.2 cm^2 for the device fabrication.

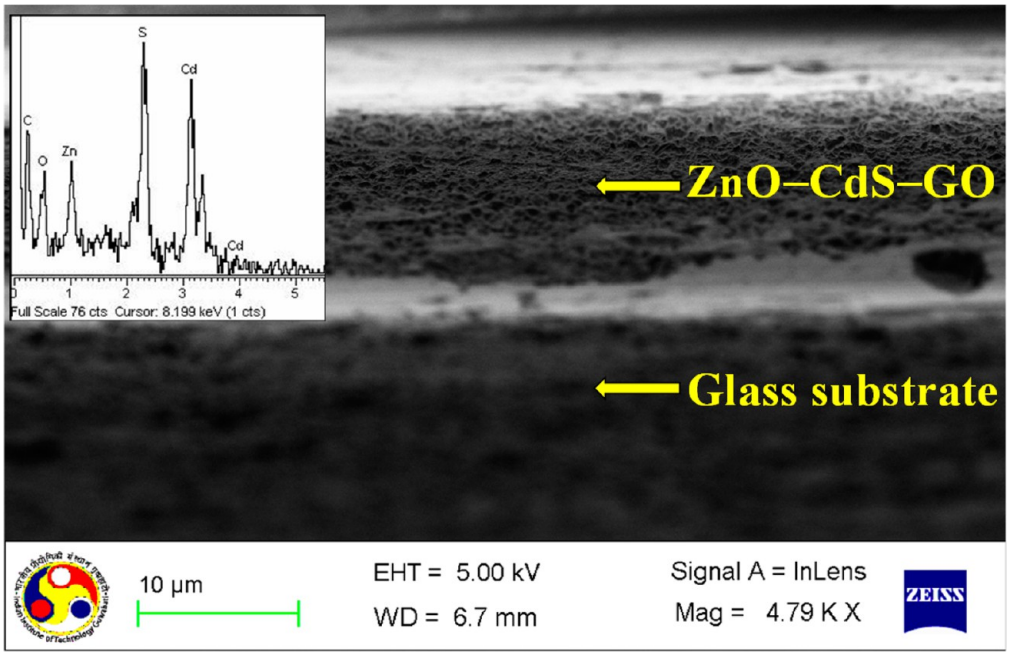

Figure 1. Field-emission scanning electron microscopy (FESEM) image of the cross-sectional view of ZnO−CdS−GO photoanode fabricated on a glass substrate showing a ZnO−CdS−GO layer. Inset shows the energy-dispersive X-ray (EDX) pattern of the ZnO−CdS−GO layer of the fabricated photoanode.

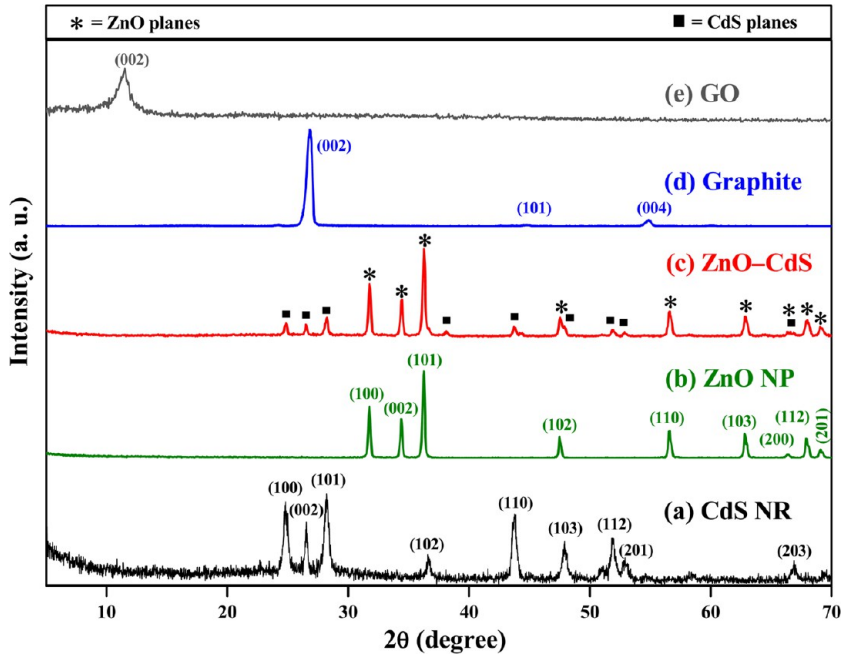

Figure 2. Powder X-ray diffraction (XRD) patterns for (a) CdS nanorods (NRs), (b) ZnO nanoparticles (NPs), (c) ZnO−CdS composite, (d) graphite, and (e) graphene oxide (GO).

Hydrothermally synthesized ZnO−CdS−GO (5.0 g) was taken in an agate mortar and ground for 1 h with *tert*-butanol (added dropwise time to time) to obtain a paste and then the paste was coated over the ITO film using the doctor blade technique. The solvent was then evaporated by drying in an electronic oven overnight at 40 °C. The measured thickness of the ZnO−CdS−GO layer was found to be within a range of 10−15 μm under the surface profilometer. This ITO/ZnO−CdS−GO acted as the photoanode for the device. A Pt-coated ITO substrate or Ag-deposited glass substrate then were used as the counter electrodes for the device characterization. To prepare the Pt counter electrode, H_2PtCl_6 solution in ethanol (2 mg Pt/mL) was spin-coated on a precleaned ITO substrate. The ITO substrate that was coated with Pt solution was then placed in a muffle furnace at 450 °C (heating ramp of 5 °C/min) for 15 min and cooled to room temperature naturally. For the Ag electrode deposition, first, glass substrates were cleaned in isopropanol and acetone under the ultrasonic treatment for 15 min, dried by blowing argon gas, and subjected to ozone treatment for 10 min. Silver was then deposited by thermal evaporation in a Vinci Meca 2000 thermal evaporator at a deposition rate of 2.0 Å/s under a vacuum of $\sim 10^{-7}$ mbar. The photovoltaic cells were constructed by placing the counter electrode on the top of the photoanode. A drop of sulfide/polysulfide (S_2^-/S_n^{2-})

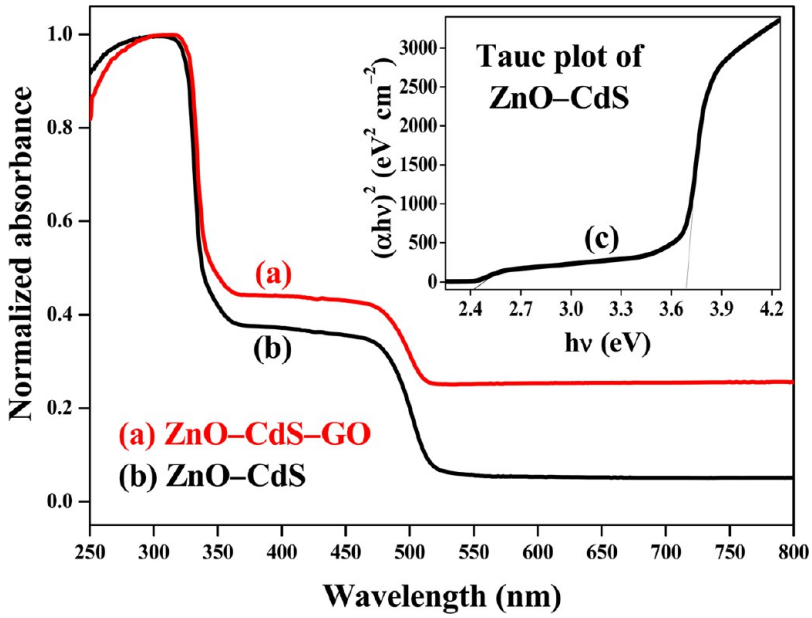

Figure 3. UV-Vis diffuse reflectance spectroscopy (DRS) absorption spectra of (a) ZnO−CdS−GO (red line) and (b) ZnO−CdS (black line). Trace (c), in the inset, shows the Tauc plot for ZnO−CdS.

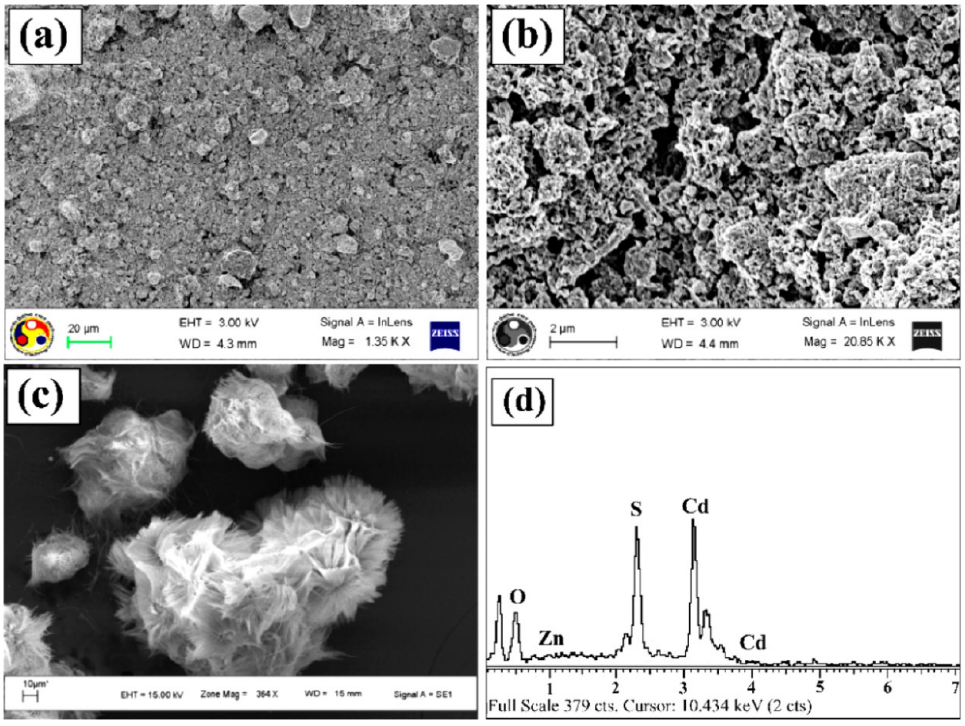

Figure 4. Scanning electron microscopy (SEM) images of (a, b) ZnO−CdS−GO composite layer painted on the ITO substrate and (c) bare ZnO−CdS at higher magnification. (d) Energy-dispersive X-ray spectroscopy (EDX) pattern for the ZnO−CdS composite.

electrolyte solution was injected to complete the device. Electrolyte solution was prepared by dissolving 2M S and 2M Na_2S in distilled water. The photocurrent and IPCE measurements were then carried out. The effect of GO in the device performance was investigated by fabricating a GO-free device constructed with ITO/ZnO−CdS photoanode and Pt/Ag counter electrodes. For the photoanode fabrication, ZnO−CdS paste was prepared by grinding ZnO−CdS in *tert*-butanol for 1 h. It was then painted on precleaned ITO-coated glass substrate using the doctor blade method to make a film ∼10−15 μm thick and then dried at 40 °C overnight. Hereafter, the fabricated GO-based and GO-free devices are abbreviated as ZCGO-Pt (ITO/ZnO−CdS−GO/Pt), ZC-Pt (ITO/ZnO−CdS/Pt), ZCGO-Ag (ITO/ZnO−CdS−GO/Ag), and ZC-Ag (ITO/ZnO−CdS/Ag). In order to have a better understanding about the layer interfaces and thickness of the individual layers, we have performed cross-sectional FESEM analysis of the photoanode. For FESEM, the ZnO−CdS−GO paste was painted on a glass substrate (precleaned under ultrasonic treatment in isopropanol and acetone). The sample was dried overnight at 40 °C and then mounted at an angle of 60° on the sample holder of the instrument. The imaging was carried out by tilting the sample holder during analysis. The estimated thickness of the coated layer is found to be ∼10−12 μm, as shown in Figure 1. The

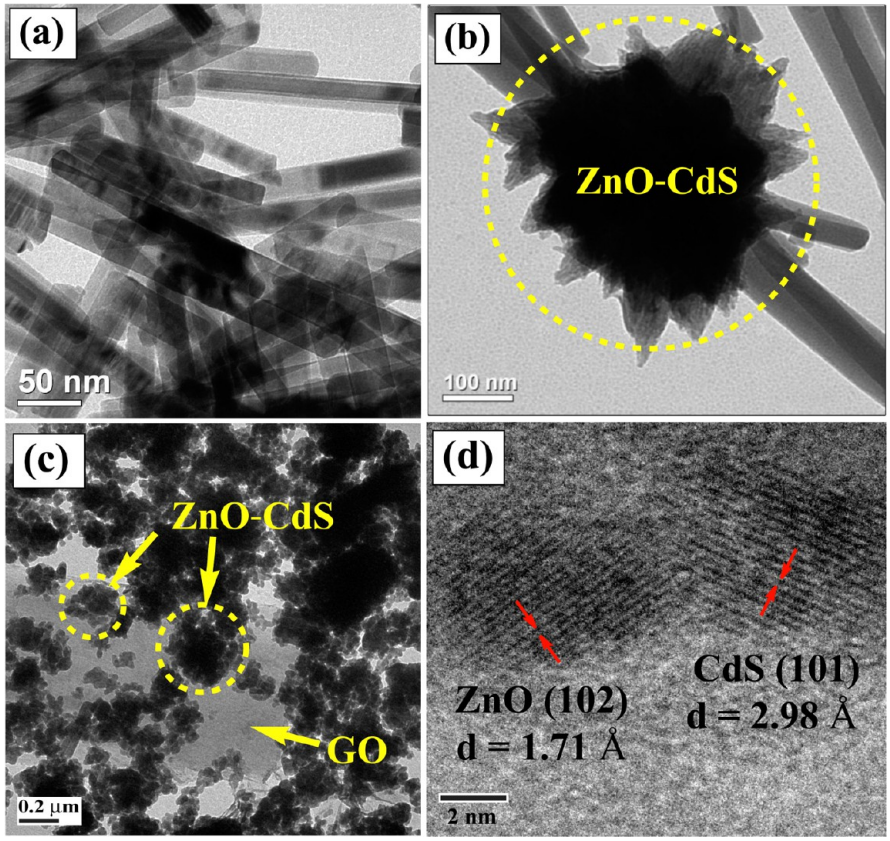

Figure 5. Transmission electron microscopy (TEM) images of (a) CdS NRs, (b) ZnO−CdS, and (c) ZnO−CdS−GO; (d) high-resolution TEM (HRTEM) image of ZnO−CdS−GO.

thickness of the layers were further confirmed by the surface profilometer.

3. RESULTS AND DISCUSSION

3.1. Powder X-ray Diffraction Analysis. Powder X-ray diffraction (XRD) patterns for CdS NRs, ZnO NPs, ZnO−CdS composite, graphite, and GO are depicted in Figure 2. From trace (a) in Figure 2, the crystal planes (100), (002), (101), (102), (110), (103), (112), (201), and (203) can be indexed to the formation of hexagonal CdS NRs with cell constant parameters of a = 0.4136 nm and c = 0.6713 nm (JCPDS File Card No. 06-0314). Trace (b) in Figure 2 shows the diffractogram for ZnO NPs, where the crystal planes (100), (002), (101), (102), (110), (103), (200), (112), and (201) are indexed to the formation of hexagonal phase ZnO with cell constants of a = 0.3249 nm and c = 0.5205 nm (JCPDS File Card No. 05-0664). Trace (c) in Figure 2 shows that the diffraction peaks for CdS are retained in the diffractogram for the ZnO−CdS composite. It clearly reveals that the structure and crystalline phases of freestanding CdS NRs are retained even after they are grown onto ZnO NPs. The *P*63*mc* space group symmetry of both CdS NR and ZnO NPs remain same in the hydrothermally synthesized ZnO−CdS composite. Traces (d) and (e) in Figure 2 show the XRD patterns for graphite and GO, respectively, where the crystal planes (002), (101), and (004) are indexed to graphite and (002) in indexed to GO.

3.2. UV-Vis Diffuse Reflectance Absorption Spectra. The UV-Vis DRS spectra of the ZnO−CdS and ZnO−CdS−GO composites are recorded to examine the light-harvesting abilities of the samples; these are presented in Figure 3. The absorbance values for both samples are plotted against a wavelength range of 200−800 nm. Both samples have shown almost the same absorption profile that corresponds to the band energy components of the individual systems. As can be seen, there are two distinct absorption edges, at ∼330 and ∼500 nm in each of the curves. A slight red shift in the absorption steep of ZnO−CdS occurs in the presence of GO. This is attributed to the charge delocalization due to electronic interaction of GO to ZnO−CdS. Also, GO influences the enhancement in the absorption of ZnO−CdS in the visible region.[42,43] Figure 3c represents the Tauc plot for ZnO−CdS composite to evaluate the band gap of the materials, where $(\alpha h\nu)^2$ is plotted as a function of photon energy ($h\nu$). The estimated band-gap energies for the ZnO−CdS composite are found to be ∼3.7 and ∼2.5 eV, which corresponds to the individual band gaps of ZnO and CdS components in the composite, respectively.

3.3. Materials Morphology. The representative SEM images of hydrothermally synthesized ZnO−CdS−GO composite grown over the ITO substrate are shown in Figures 4a and 4b. A higher-magnification image of the bare ZnO−CdS is shown in Figure 4c, which clearly demonstrates that the CdS NRs are radially grown on the ZnO NPs. Figure 4d represents the energy-dispersive X-ray spectroscopy (EDX) of ZnO−CdS that confirms the presence of the elements Cd, S, Zn, and O. Thus, the ZnO-templated one-dimensional (1-D) growth of CdS NRs has been indicated by the SEM images.

The nanocomposites were further studied by TEM and high-resolution TEM (HRTEM). Figure 5a shows the TEM image of CdS NRs, whereas Figure 5b represents the star-shaped image of the ZnO−CdS composite, which exhibits a diameter

of ~500 nm for the ZnO−CdS core−shells. The star shape arises due to the hierarchical alignment of CdS NRs over ZnO NPs.[39] The sample preparation for TEM analysis was carried out by dispersing the solid sample in acetone for 30 min under ultrasonic treatment. The rod-shaped structures that are seen near the star in Figure 5b are the bare CdS NRs that are coming out of the hierarchical arrangement under the ultrasonic treatment for TEM sample preparation. Figures 5c and 5d represent the TEM and HRTEM images of the ZnO−CdS−GO composite. In the HRTEM image, clearly well-defined lattice fringes with the interplanar *d*-spacing values in the ZnO−CdS−GO composite are measured to be ~0.17 and ~0.29 nm, which are assignable to the interplanar spacing of (102) and (101) planes of ZnO and CdS, respectively.

3.4. Steady-State Fluorescence and Time-Resolved Photoluminescence (PL) Studies. The recorded steady-state fluorescence spectra for as-synthesized ZnO−CdS composites in the presence and absence of GO are represented in Figure 6.

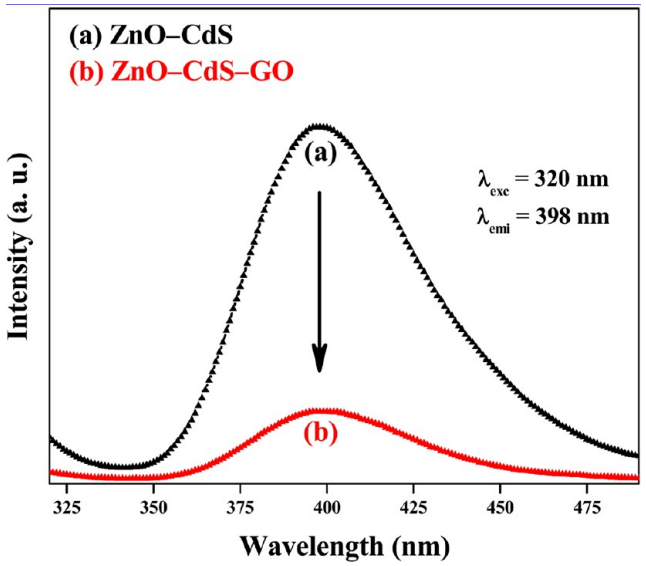

Figure 6. Steady-state fluorescence spectra for hydrothermally synthesized ZnO−CdS composites in presence of (a) 0.0 wt % GO and (b) 1.0 wt % GO at an excitation wavelength of 320 nm.

As can be seen, trace (a) in Figure 6 shows a strong fluorescence emission band (λ_{emi}) at 398 nm for the ZnO−CdS composite upon excitation (λ_{exc}) at 320 nm. This confirms that the electron−hole recombination gives stronger PL in the ZnO−CdS composite, compared to the ZnO−CdS−GO composite. This indicates the presence of electronic interactions between ZnO−CdS and GO that incorporates the inhibited photoinduced electron−hole recombination, which is further confirmed by time-resolved photoluminescence (TRPL) spectra and the exciton lifetime studies. The TRPL spectra of ZnO−CdS and ZnO−CdS−GO composites are represented by traces (a) and (b) in Figure 7.

The interaction of GO with the ZnO−CdS composite quenches the PL lifetime of the ZnO−CdS composite through charge-transfer processes. Son et al. proposed a similar mechanism for quenching the PL lifetime of ZnO in the presence of graphene.[44] The functional groups carboxyl (−COOH), hydroxyl (−OH), and epoxy of GO can easily bind to the semiconductors under hydrothermal conditions, which makes the efficient transfer of photoexcited electrons

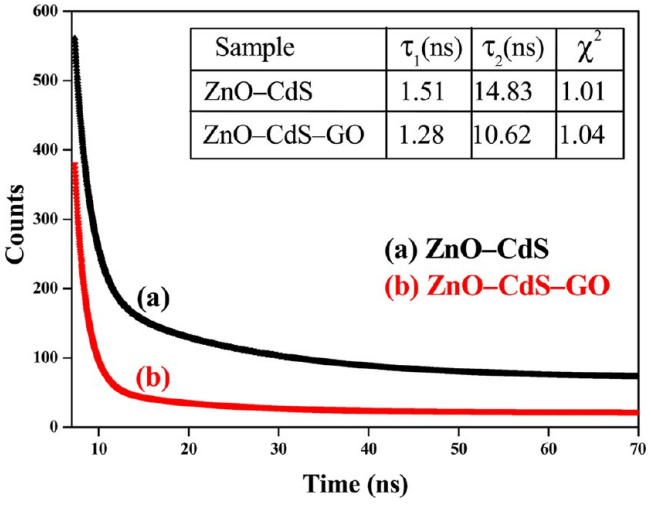

Figure 7. Time-resolved photoluminescence (TRPL) spectra for the ZnO−CdS composite in the presence of (a) 0.0 wt % GO and (b) 1.0 wt % GO at an excitation wavelength of 405 nm.

possible from ZnO−CdS to GO and, hence, the static quenching in PL lifetime is observed. This is extensively examined by the exciton lifetime measurements for GO-free and GO-loaded ZnO−CdS composites (see inset to Figure 7), calculated by plotting the TRPL curves fitted with a biexponential function. The biexponential fitting curve gives the average values τ_1 and τ_2, which are, respectively, the fast and slow emission decay lifetimes of the ZnO−CdS composite. The decay curves obtained are fitted in the function (eq 1) using FAST software provided by Edinburgh Instruments:

$$I(t) = \sum \alpha_i \exp\left(-\frac{t}{\tau_i}\right) \quad (1)$$

where α_i is the initial intensity of the decay component *i* having a lifetime of *t*. The average lifetimes τ_1 and τ_2 of ZnO−CdS are calculated using eq 2.

$$\langle\tau\rangle = \frac{\sum_i \alpha_i \tau_i^2}{\sum_i \alpha_i \tau_i} \quad (2)$$

The coupling of GO notably decreases the two exciton lifetimes of the ZnO−CdS emission from 1.51 ns to 1.28 ns (for τ_1) and from 14.83 ns to 10.62 ns (for τ_2).

3.5. Raman Spectra. Figure 8 depicts the room-temperature Raman spectra of the thin films prepared from (a) ZnO−CdS (trace a), ZnO−CdS−GO (trace b) and GO (trace c), excited by a He−Ne laser operating at 514.5 nm, over the spectral range of 100−2000 cm^{-1}. As can be seen from trace (a) in Figure 8, at 0.0 wt % GO loading, there is almost no characteristic Raman intensity, whereas trace (b) in Figure 8 shows the two characteristic longitudinal optical (LO) peaks for CdS at 298 cm^{-1} and 592 cm^{-1} on 1.0 wt % loading of GO into ZnO−CdS. Trace (c) in Figure 8 shows two distinct Raman peaks at 1358 cm^{-1} and 1599 cm^{-1}, which are, respectively, the characteristic D- and G-bands for synthesized GO nanosheets. It is worthy of notice that, in comparison to the ZnO−CdS−GO composite, the observed Raman spectrum shows no intense peaks for bare ZnO−CdS. The visible−Raman spectroscopy technique has a drawback in that it characterizes luminescent samples in the presence of fluorescence background interference.[45] Basically, more intense and broad

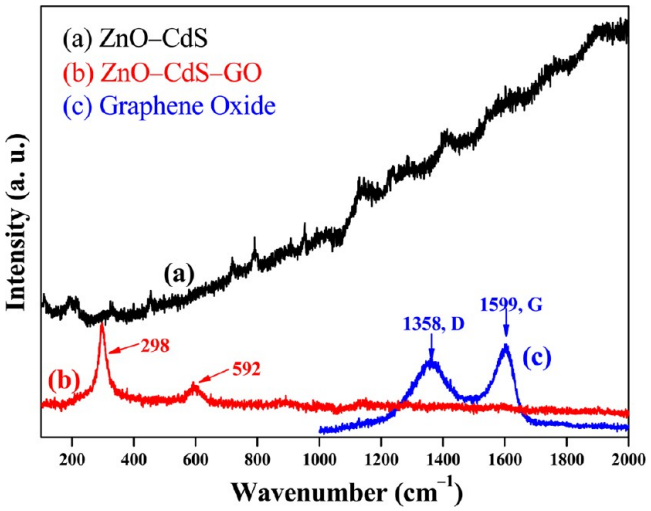

Figure 8. Raman spectra for the thin films of ZnO–CdS (trace a, black line), ZnO–CdS–GO (trace b, red line), and GO (trace c, blue line) at an excitation wavelength of 514.5 nm by a He–Ne laser.

fluorescence emission peaks, compared to the Raman scattering, hinders the Raman signal of fluorescent samples. One of the best ways to obtain the Raman signal is to remove the luminescent species. In the present work, the 1.0 wt % loading of GO into ZnO–CdS sufficiently quenches the fluorescence emission arising from the ZnO–CdS composite and thereby exhibits the Raman peaks. This is in agreement to the fluorescence quenching and TRPL studies to conclude the presence of electronic interaction between GO and ZnO–CdS.

3.6. Photovoltaic Performance. The photovoltaic properties of the fabricated GO-based device ZCGO-Pt is monitored by the current density (J_{sc}), as a function of applied voltage (V). The role of GO in device performance, implying the hybrid ternary ZnO–CdS–GO photoanode, is evaluated by comparing the J–V curves for GO-free devices. The characteristic J–V curves for the devices at 100 mW/cm^2 under AM 1.5G solar illumination are shown in Figure 9. The solar cell parameters of

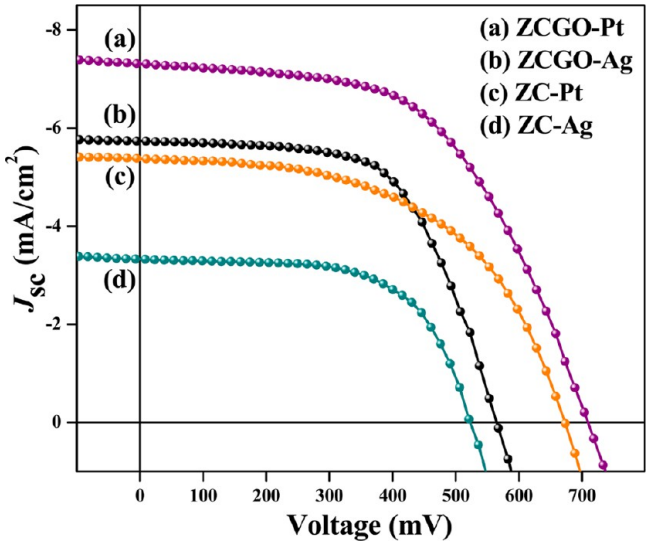

Figure 9. Current density–voltage (J–V) curve for the photovoltaic devices: ZCGO-Pt (trace a), ZCGO-Ag (trace b), ZC-Pt (trace c), and ZC-Ag (trace d) under AM 1.5G solar illumination.

the fabricated devices, including the short-circuit current density (J_{sc}), open-circuit voltage (V_{oc}), fill factor (FF), power conversion efficiency (PCE, η), and maximum IPCE are summarized in Table 1. It is observed that the cell ZCGO-Pt constructed with the hybrid ZnO–CdS–GO photoanode exhibited the highest J_{sc} value (~7.3 mA/cm^2) and the maximum PCE ($\eta \approx 2.8\%$), with $V_{oc} \approx 703$ mV and FF ≈ 54.6%, using the Pt counter electrode. The efficiency value decreases to ~1.92% with a J_{sc} value of ~5.3 mA/cm^2 in the GO-free ZC-Pt device, along with $V_{oc} \approx 672$ mV and FF ≈ 54.2%. It is noteworthy that, compared to the ZC-Pt cell having GO-free photoanode, the presence of GO significantly increases the efficiency of the ZCGO-Pt cell by ~47% and increases the J_{sc} value by ~38%. The drastic increment in the device performance confirms that 1.0 wt % loading of GO to ZnO–CdS improves the electron transfer in the device. Similarly, with Ag-based counter electrode devices, an increment in the PCE from 1.08% to 1.96% has been observed in the presence of GO, whereas the J_{sc} value increases from ~3.3 mA/cm^2 to ~5.7 mA/cm^2, V_{oc} increases from 523 mV to 565 mV, and FF increases from 61.7% to 63.2%. In the device architecture, ZnO–CdS–GO photoanode consists of ZnO–CdS well-embedded in GO sheets; such a configuration facilitates the charge transfer within the system. Moreover, the nanodimension of crystalline ZnO and CdS in the composite enhances the migration of electrons and holes to their surface more rapidly under the solar illumination.[46] Interestingly, the band alignments of CdS, ZnO, and GO allows the electrons and holes to be separated within the hybrid ZnO–CdS–GO photoanode itself, thereby reducing the charge recombination process and making headway with the photovoltaic performance.[18,19,47] It is observed that the Pt-based devices have shown better photovoltaic performance over Ag counter electrodes. Increments in J_{sc} (~2 mA/cm^2) and V_{oc} (~130 mV) are observed in the ZC-Pt and ZCGO-Pt devices, compared to ZC-Ag and ZCGO-Ag devices. The increased current density, in the case of Pt, is due to its higher work function (~6.3 eV) than that of Ag (~4.7 eV). This can be explained based on the favorable electron transport to the Fermi level of metal electrode, because of the higher work function of the counter electrode. On the other hand, the V_{oc} value of a semiconductor-sensitized solar cell (SSSC) depends on the potential difference between the quasi-Fermi level of the semiconductor material and the work function of the electrolyte. Moreover, we have observed that the Ag counter electrode has stability issues, when it is in direct contact with the active layer. The formation of Ag_2S from Ag, in the presence of a sulfide/polysulfide electrolyte, has been observed which is evident from powder XRD analysis of the samples collected from the solar cell before and after the electrolyte activation. (See Figure S1 in the Supporting Information). Although the formation of Ag_2S is significantly less, it shows a greater effect in altering the charge migration and, hence, the electron–hole recombination to lower the V_{oc} in Ag-based devices, compared to the Pt. It is also observed that the reduced recombination of electrons and holes in the presence of GO induces an increase in V_{oc}, compared to that observed in the GO-free devices.

To estimate the photocurrent characteristics of the fabricated SSSCs having ZnO–CdS–GO hybrid and ZnO–CdS photoanodes, the IPCE as a function of wavelength are measured under short-circuit conditions. Figure 10 illustrates the improved photon-to-current response of the fabricated devices

Table 1. Short-Circuit Photocurrent Density (J_{sc}), Open-Circuit Voltage (V_{oc}), Fill Factor (FF), Power Conversion Efficiency (η), and Maximum IPCE ($IPCE_{max}$) Values for the Fabricated Solar Cells with Respect to Different Photoanodes and Counter Electrodes

solar cell	photoanode	counter electrode	J_{sc} (mA/cm^2)	V_{oc} (mV)	FF (%)	η (%)	$IPCE_{max}$ (%)
ZC-Pt	ZnO−CdS	Pt	5.3	672	54.2	1.92	18
ZCGO-Pt	ZnO−CdS−GO	Pt	7.3	703	54.6	2.82	22
ZC-Ag	ZnO−CdS	Ag	3.3	523	61.7	1.08	11
ZCGO-Ag	ZnO−CdS−GO	Ag	5.7	565	63.2	1.96	13

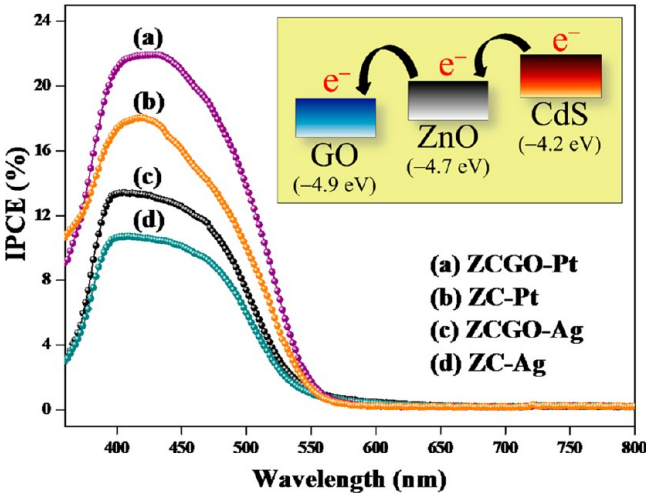

Figure 10. Incident photon-to-current conversion efficiency (IPCE) plots for the photovoltaic devices: ZCGO-Pt (~22%) (trace a), ZC-Pt (~18%) (trace b), ZCGO-Ag (~13%) (trace c), and ZC-Ag (~11%) (trace d). Inset shows the electron transfer within the hybrid photoanode ZnO−CdS−GO based on their band alignments.

in the presence of GO in the photoanode over the GO-free cell. As can be seen from Figure 10, the ZCGO-Pt cell shows the maximum IPCE value up to ~22%, whereas the corresponding GO-free cell exhibited an IPCE of ~18% (ZC-Pt).

In principle, the IPCE of ZnO−CdS−GO-based devices accounts for the efficiencies of (i) light harvesting by CdS sensitizer, (ii) electron injection within the components of hybrid ZnO−CdS−GO, and (iii) photoexcited electron collection by the ITO substrate. Therefore, it is expected to acquire the maximum IPCE value at the specific wavelength region where the UV-Vis absorption is maximum. As shown in Figure 3, the UV-Vis absorptions of the ZnO−CdS and ZnO−CdS−GO composites are maximum in the wavelength range of 330−550 nm. The obtained IPCE plots also ascribed the ability to convert photons to electrons within the same wavelength range. This is attributed to the proximal band alignments of ZnO and CdS, as shown in the inset to Figure 10, which results in the electron transfer from CdS to ZnO. Essentially, the presence of GO enhances the electron migration and separation due to the electronic interaction of GO with ZnO and CdS.[19,43] On the other hand, lower IPCE values for the GO-free SSSC indicates that the physical separation of the electron−hole pair is poor in the absence of GO. Thus, the high IPCE of the SSSCs fabricated with ZnO−CdS−GO photoanodes results in a high photocurrent density and high photovoltaic performance. Similar proficiency in the IPCE from ~11% to ~13% has been observed for the ZnO−CdS−GO hybrid, compared to GO-free device having Ag counter electrodes.

CONCLUSIONS

In conclusion, the present work manifests the design and development of photovoltaic device based on hierarchical ternary ZnO−CdS−GO composites. The effect of graphene oxide (GO) in the performance of a semiconductor-sensitized solar cell, using CdS as a sensitizer, has been explored. The hybrid ZnO−CdS−GO has demonstrated an enhanced electron transfer based on the band alignments of ZnO, CdS, and GO entities within the composite. Graphene oxide acts as an electron acceptor (sink) for better separation of charge generated under photoexcitation. The hydrothermal treatment to synthesize ZnO−CdS−GO practically offers an inexpensive way to achieve electronic coupling of the functional groups of GO with ZnO and CdS. This work further gives scope to investigate ternary systems having different band alignments, wherein effective charge transfer is possible for solar energy conversion applications.

ASSOCIATED CONTENT

Supporting Information

Powder XRD patterns of the fabricated Ag counter electrode before and after the treatment with sulfide/polysulfide electrolyte (Figure S1). This material is available free of charge via the Internet at http://pubs.acs.org.

AUTHOR INFORMATION

Corresponding Author

*Tel: +91-361-2582320. Fax: +91-3612582349. E-mail: mq@iitg.ernet.in.

Notes

The authors declare no competing financial interest.

ACKNOWLEDGMENTS

We acknowledge Department of Science and Technology (DST), India for financial support via the sponsored projects Nos. DST/SR/S1/IC-25/2009 and DST/TSP/2009/23. D.B. and M.Q. thank Dr. Ziyauddin Khan for his help in the characterization of compounds using SEM and TEM. Infrastructure and instrument facilities from Indian Institute of Technology Guwahati, India, is duly acknowledged.

REFERENCES

(1) Huang, Y.; Duan, X.; Wei, Q.; Lieber, C. M. *Science* **2001**, *291*, 630−633.
(2) Hagfeldt, A.; Boschloo, G.; Sun, L.; Kioo, L.; Pettersson, H. *Chem. Rev.* **2010**, *110*, 6595−6663.
(3) O'Regan, B.; Gratzel, M. *Nature* **1991**, *353*, 737−740.
(4) Gratzel, M. *Nature* **2001**, *414*, 338−344.
(5) Green, M. A.; Emery, K.; King, D. L.; Hishikawa, Y.; Warta, W. *Prog. Photovoltaics* **2006**, *14*, 455−461.
(6) Sun, W. T.; Yu, Y.; Pan, H. Y.; Gao, X. F.; Chen, Q.; Peng, L. M. *J. Am. Chem. Soc.* **2008**, *130*, 1124−1125.

(7) Gao, J. B.; Luther, J. M.; Semonin, O. E.; Ellingson, R. J.; Nozik, A. J.; Beard, M. C. *Nano Lett.* **2011**, *11*, 1002−1008.
(8) Robel, I.; Subramanian, V.; Kuno, M.; Kamat, P. V. *J. Am. Chem. Soc.* **2006**, *128*, 2385−2393.
(9) Seabold, J. A.; Shankar, K.; Wilke, R. H. T.; Paulose, M.; Varghese, O. K.; Grimes, C. A.; Choi, K. S. *Chem. Mater.* **2008**, *20*, 5266−5273.
(10) Das, K.; De, S. K. *J. Phys. Chem. C* **2009**, *113*, 3494−3501.
(11) Cho, Y. J.; Kim, H. S.; Park, J. *ACS Nano* **2010**, *4*, 3789−3800.
(12) Greene, L. E.; Law, M.; Yuhas, B. D.; Yang, P. *J. Phys. Chem. C* **2007**, *111*, 18451−18456.
(13) Zhang, Y.; Wang, L. W.; Mascarenhas, A. *Nano Lett.* **2007**, *7*, 1264−1269.
(14) Hochbaum, A. I.; Yang, P. *Chem. Rev.* **2010**, *110*, 527−546.
(15) Han, S. E.; Chen, G. *Nano Lett.* **2010**, *10*, 1012−1015.
(16) McAlpine, M. C.; Friedman, R. S.; Jin, S.; Lin, K. H.; Wang, W. U.; Lieber, C. M. *Nano Lett.* **2003**, *3*, 1531−1535.
(17) Wang, W.; Zhao, Q.; Laurent, K.; Leprince-Wang, L.; Liao, Z.-M.; Yu, D. *Nanoscale* **2012**, *4*, 261−268.
(18) Khan, Z.; Chetia, T. R.; Vardhaman, A. K.; Barpuzary, D.; Sastri, C. V.; Qureshi, M. *RSC Adv.* **2012**, *2*, 12122−12128.
(19) Luo, Q.-P.; Yu, X.-Y.; Lei, B.-X.; Chen, H.-Y.; Kuang, D.-B.; Su, C.-Y. *J. Phys. Chem. C* **2012**, *116*, 8111−8117.
(20) Lee, Y.-Y.; Tu, K.-H.; Yu, C.-C.; Li, S.-S.; Hwang, J.-Y.; Lin, C.-C.; Chen, K.-H.; Chen, L.-C.; Chen, H.-L.; Chen, C.-W. *ACS Nano* **2011**, *5*, 6564−6570.
(21) Yang, H.; Guai, G. H.; Guo, C.; Song, Q.; Jiang, S. P.; Wang, Y.; Zhang, W.; Li, C. M. *J. Phys. Chem C* **2011**, *115*, 12209−12215.
(22) Mathkar, A.; Tozier, D.; Cox, P.; Ong, P.; Galande, C.; Balakrishnan, K.; Reddy, A. L. M.; Ajayan, P. M. *J. Phys. Chem. Lett.* **2012**, *3*, 986−991.
(23) Eda, G.; Mattevi, C.; Yamaguchi, H.; Kim, H.; Chhowalla, M. *J. Phys. Chem. C* **2009**, *113*, 15768−15771.
(24) Kamat, P. V. *J. Phys. Chem. Lett.* **2010**, *1*, 520−527.
(25) Kamat, P. V. *J. Phys. Chem. Lett.* **2011**, *2*, 242−251.
(26) Lightcap, I. V.; Kamat, P. V. *Acc. Chem. Res.* **2013**, *46*, 2235−2243.
(27) Bao, J.; Zimmler, M. A.; Capasso, F.; Wang, X.; Ren, Z. F. *Nano Lett.* **2006**, *6*, 1719−1722.
(28) Hayashi, H.; Lightcap, I. V.; Tsujimoto, M.; Takano, M.; Umeyama, T.; Kamat, P. V.; Imahori, H. *J. Am. Chem. Soc.* **2011**, *133*, 7684−7687.
(29) She, J.; Xiao, Z.; Yang, Y.; Deng, S.; Chen, J.; Yang, G.; Xu, N. *ACS Nano* **2008**, *2*, 2015−2022.
(30) Lu, X.-H.; Wang, D.; Li, G.-R.; Su, C.-Y.; Kuang, D.-B.; Tong, Y.-X. *J. Phys. Chem. C* **2009**, *113*, 13574−13582.
(31) Kim, H.; Jeong, H.; An, T. K.; Park, C. E.; Yong, K. *ACS Appl. Mater. Interfaces* **2013**, *5*, 268−275.
(32) Rakshit, T.; Mondal, S. P.; Manna, I.; Ray, S. K. *ACS Appl. Mater. Interfaces* **2012**, *4*, 6085−6095.
(33) Wang, X.; Liu, G.; Chen, Z.-G.; Li, F.; Wang, L.; Lu, G. Q.; Cheng, H.-M. *Chem. Commun.* **2009**, 3452−3454.
(34) Tak, Y.; Hong, S. J.; Lee, J. S.; Yong, K. *J. Mater. Chem.* **2009**, *19*, 5945−5951.
(35) Leschkies, K. S.; Divakar, R.; Basu, J.; Enache-Pommer, E.; Boercker, J. E.; Carter, C. B.; Kortshagen, U. R.; Norris, D. J.; Aydil, S. A. *Nano Lett.* **2007**, *7*, 1793−1798.
(36) Emin, S.; Fanetti, M.; Abdi, F. F.; Lisjak, D.; Valant, M.; van de Krol, R.; Dam, B. *ACS Appl. Mater. Interfaces* **2013**, *5*, 1113−1121.
(37) Lightcap, V.; Kamat, P. V. *J. Am. Chem. Soc.* **2012**, *134*, 7109−7116.
(38) Khan, D.; Barpuzary, D.; Baswant, O.; Sutradhar, S.; Qureshi, M. *Mater. Lett.* **2011**, *65*, 1168−1171.
(39) Barpuzary, D.; Khan, Z.; Vinothkumar, N.; De, M.; Qureshi, M. *J. Phys. Chem. C* **2012**, *116*, 150−156.
(40) Sun, B.; Hao, Y.; Guo, F.; Cao, Y.; Zhang, Y.; Li, Y.; Xu, D. *J. Phys. Chem. C* **2012**, *116*, 1395−1400.
(41) Becerril, H. A.; Mao, J.; Liu, Z.; Stoltenberg, R. M.; Bao, Z.; Chen, Y. *ACS Nano* **2008**, *2*, 463−470.
(42) Zhang, H.; Lv, X.; Li, Y.; Wang, Y.; Li, J. *ACS Nano* **2010**, *4*, 380−386.
(43) Hou, J.; Wang, Z.; Kan, W.; Jiao, S.; Zhu, H.; Kumar, R. V. *J. Mater. Chem.* **2012**, *22*, 7291−7299.
(44) Son, D. I.; Kwon, B. W.; Park, D. H.; Seo, W.-S.; Yi, Y.; Angadi, B.; Lee, C.-L.; Choi, W. K. *Nat. Nanotechnol.* **2012**, *7*, 465−471.
(45) Chen, J.; Feng, Z.; Ying, P.; Li, C. *J. Phys. Chem. B* **2004**, *108*, 12669−12676.
(46) Ashokkumar, M. *Int. J. Hydrogen Energy* **1998**, *23*, 427−438.
(47) Li, S.-S.; Tu, K.-H.; Lin, C.-C.; Chen, C.-W.; Chhowalla, M. *ACS Nano* **2010**, *4*, 3169−3174.